Lightweight, Superelastic, and Hydrophobic Polyimide Nanofiber /MXene Composite Aerogel for Wearable Piezoresistive Sensor and Oil/Water Separation Applications

Hu Liu,* Xiaoyu Chen, Yanjun Zheng, Dianbo Zhang, Ye Zhao, Chunfeng Wang, Caofeng Pan,* Chuntai Liu,* and Changyu Shen

Inspired by the ultralight and structurally robust spider webs, flexible nanofibril-assembled aerogels with intriguing attributes have been designed for achieving promising performances in various applications. Here, conductive polyimide nanofiber (PINF)/MXene composite aerogel with typical "layer-strut" bracing hierarchical nanofibrous cellular structure has been developed via the freeze-drying and thermal imidization process. Benefiting from the porous architecture and robust bonding between PINF and MXene, the PINF/MXene composite aerogel exhibits an ultralow density (9.98 mg cm^{-3}), intriguing temperature tolerance from −50 to 250 °C, superior compressibility and recoverability (up to 90% strain), and excellent fatigue resistance over 1000 cycles. The composite aerogel can be used as a piezoresistive sensor, with an outstanding sensing capacity up to 90% strain (corresponding 85.21 kPa), ultralow detection limit of 0.5% strain (corresponding 0.01 kPa), robust fatigue resistance over 1000 cycles, excellent piezoresistive stability and reproductivity in extremely harsh environments. Furthermore, the composite aerogel also exhibits superior oil/water separation properties such as high adsorption capacity (55.85 to 135.29 g g^{-1}) and stable recyclability due to its hydrophobicity and robust hierarchical porous structure. It is expected that the designed PINF/MXene composite aerogel can supply a new multifunctional platform for human bodily motion/physical signals detection and high-efficient oil/water separation.

1. Introduction

With the foreseeable prosperity of artificial intelligence, high-performance pressure sensors with the attributes of lightweight, mechanical compliance, high sensitivity, fast response, wide response range, and stability have been emerging, promising a myriad of applications such as artificial prosthetics, smart robots, electronic skin, and wearable electronics.[1–7] A plenty of pressure sensors made of the traditional metals and inorganic semiconductors have been presented, showcasing the advantages of high sensitivity, fast response, and good stability,[8–10] however, their rigidity and limited sensing range along with the processing complexity and high costs impede the practical applications,[11] pushing the development of the flexible high-performance pressure sensors with a simple and cost-effective approach.

Targeting this issue, the pressure sensors based on the different mechanisms including piezoresistance,[12] capacitance,[13] piezoelectricity,[14] and triboelectricity[5] have been proposed, among which the piezoresistive pressure sensors have been proved to be the promising candidates due to their merits of easy processing, simple structure, good flexibility, and convenient signal collection.[15–19] Generally, the piezoresistive pressure sensors are enabled by the conductive polymer composites (CPCs), which immediately transduce the external pressure into resistance change induced by the rearrangement of the conductive networks within CPCs. CPCs are usually fabricated by combining the conductive fillers with the flexible polymer matrixes and endowed with a designed structure via proper processing techniques. Recently, CPCs with

Prof. H. Liu, X. Chen, Dr. Y. Zheng, D. Zhang, Y. Zhao,
Prof. C. Liu, Prof. C. Shen
Ministry of Education Key Laboratory of Materials Processing
and Mold (Zhengzhou University)
National Engineering Research Center for Advanced
Polymer Processing Technology
Zhengzhou University
Zhengzhou, Henan 450002, China
E-mail: liuhu@zzu.edu.cn; ctliu@zzu.edu.cn

The ORCID identification number(s) for the author(s) of this article can be found under https://doi.org/10.1002/adfm.202008006.

Prof. H. Liu, Prof. C. Wang, Prof. C. Pan
Beijing Institute of Nanoenergy and Nanosystems
Chinese Academy of Sciences
National Center for Nanoscience and Technology (NCNST)
Beijing 100083, China
E-mail: cfpan@binn.cas.cn

Prof. C. Wang
College of Physics and Optoelectronic Engineering
Shenzhen University
Shenzhen 518060, China

**ADVANCED
SCIENCE NEWS**
www.advancedsciencenews.com

**ADVANCED
FUNCTIONAL
MATERIALS**
www.afm-journal.de

typical 3D architecture are considered to be the most ideal candidate for piezoresistive sensor based on their low density, high porosity, and good elasticity.[20–24] A series of CPCs based pressure sensors with 3D structure, including thermoplastic polyurethane (TPU)/carbon nanotube foam,[15] TPU/graphene foam,[17] water-soluble polyurethane/carbon nanotube foam[25] and polyimide/carbon nanotube aerogel,[19] have been widely investigated in our previous works. All these prepared piezoresistive sensors show good flexibility, outstanding sensing stability, and wide sensing range, however, the large residual deformation in multi-cycle process and poor detection capacity of tiny pressure/strain seriously restrict their application.[26,27] Recently, inspired by the ultralight and structurally robust and elastic spider webs, ultralight nanofibril-assembled aerogels composed of fibrous cell wall has shown great potential for the fabrication of flexible piezoresistive sensors due to their superelasticity and excellent mechanical stability.[28,29] For example, Xu et al. have fabricated a piezoresistive sensor utilizing polyimide (PI) nanofiber aerogel produced by the freeze-drying and intermolecular condensation process, which exhibits ultralow density (4.6–13.1 mg cm^{-3}), ultrahigh compressibility (99%), negligible plastic deformation, and stable cellular structure over 1000 fatigue cycles at 80% compression strain.[30] Such excellent properties were also observed in other aerogel systems such as polyacrylonitrile/SiO$_2$ fiber aerogel,[31] and konjac glucomannan/SiO$_2$ derived carbonaceous nanofibrous aerogel,[23] proving that the 3D nanofibrous aerogel could be an ideal candidate for the high-performance piezoresistive sensors without residual deformation.

In this work, conductive polyimide nanofiber (PINF)/MXene composite aerogel is fabricated through a simple freeze-drying and thermal imidization process to explore its potential application for piezoresistive sensor. The reasons for the design of PINF/MXene composite aerogel are mainly based on the following two aspects: i) the excellent comprehensive properties of PI, including high/low-temperature tolerance, high mechanical strength, chemical and radiation resistance, and good flexibility, make it to be an ideal matrix to prepare piezoresistive sensors that are applicable in various harsh environments;[32–34] and ii) 2D transition metal carbide Ti$_3$C$_2$X MXene possess metal electrical conductivity, rich surface functional groups, and good hydrophilicity, which will undoubtedly endow the designed aerogel with stable electrical property.[35–38] As a result, PINF/MXene composite aerogel with special "layer-strut" bracing hierarchical nanofibrous cellular structure is successfully prepared, exhibiting intriguing properties of extremely low density (9.98 mg cm^{-3}), stable elastic property in a wide temperature range from −50 to 250 °C, super cyclic compressibility and stable cyclic mechanical properties. All these lead to outstanding sensing performances of the as-fabricated piezoresistive sensor, including wide sensing range from 0.5–90% strain (corresponding 0.01–85.21 kPa), good fatigue resistance over 1000 cycles, outstanding piezoresistive sensing stability and reproductivity in high/low-temperature environments. Moreover, we can also confirm the versatility of the PINF/MXene composite aerogel based piezoresistive sensor for human bodily motion and physical signals detection, such as carotid pulse, inhalation/exhalation, pronunciation, head shaking, knee bending, and finger bending. Interestingly, benefiting from the hydrophobicity and robust hierarchical porous structure of our PINF/MXene composite aerogel, it is also proved to be a superior oil/water separation material with higher adsorption capacity (55.85–135.29 g g^{-1}) for various oil and organic solvents, showing its potential to be an ideal decontamination material in applications of environmental protection.

2. Results and Discussions

Figure 1A illustrates the preparation process of the PINF/MXene composite aerogel (see detail in Section 4). To verify the successful preparation of Ti$_3$C$_2$X MXene nanosheet, a series of characterizations were systematically conducted. As shown in Figure 1B,C, high quality transparent 2D MXene nanosheet with a lateral size of 600 nm and a thickness of 6 nm is successfully prepared. Figure 1D depicts the X-ray diffraction (XRD) patterns of Ti$_3$AlC$_2$ and MXene. The characteristic peaks of Ti$_3$AlC$_2$ at 9.4°, 19.0°, 34.0°, 38.7°, 38.9°, and 41.8° are assigned to the (002), (004), (101), (008), (104), and (105) crystal planes, respectively.[39,40] The strong (104) peak vanishes completely after the etching and delamination process, indicating the successful etching of Al atomic layer from Ti$_3$AlC$_2$.[41] The (002) peak of MXene displays a lower angle (6.15°) than that of Ti$_3$AlC$_2$ (9.4°), which is an evidence for the extended interlayer distance after the etching and delamination process.[42] In addition, the well-maintained sharpness of (002) peak demonstrates the high crystalline degree and good structural order of the prepared MXene.[43]

In order to obtain PINF/MXene composite aerogel with excellent mechanical properties and uniform 3D structure, the following two steps are of great importance: i) Homogeneous suspension of PINF and MXene. Here, considering the good dispersibility of MXene in water, the environmentally friendly deionized water was chosen as the ideal dispersing medium. Clearly, the resulting dark green MXene nanosheet aqueous suspension displays a significant "Tyndall effect" (Figure S1, Supporting Information) showing the formation of stable colloidal suspension due to the polar and hydrophilic functional groups (−O, −OH, −F) on its surface.[43,44] Besides, simple and effective oxygen-plasma treatment is applied to solve the problem of the inherent hydrophobicity of PINF, and its surface hydrophilicity is significantly improved (Figure S2A,B, Supporting Information). As a result, homogeneous PINF/MXene mixture is successfully obtained (Figure S2C, Supporting Information); ii) Construction of robust 3D porous structure. Water-soluble poly (amic acid) (PAA) was used as a binder to glue the dispersed PINF and MXene together during the aerogel formation process. PAA is ultimately converted into PI and welded the PINF–PINF and PINF–MXene joints after the thermal imidization process,[19] endowing the composite aerogel with good structural stability compared with that without PAA (Figure S3 and Video S1, Supporting Information). In addition, the dogtail grass could bear the obtained PINF/MXene composite aerogel without being bent, showing the lightweight merit of the prepared composite aerogel. Furthermore, the PINF/MXene composite aerogel also exhibits excellent tailorability (Figure 1E), compressibility (Figure 1F), torsionability, and bendability (Figure 1G). All these characteristics will undoubtedly endow
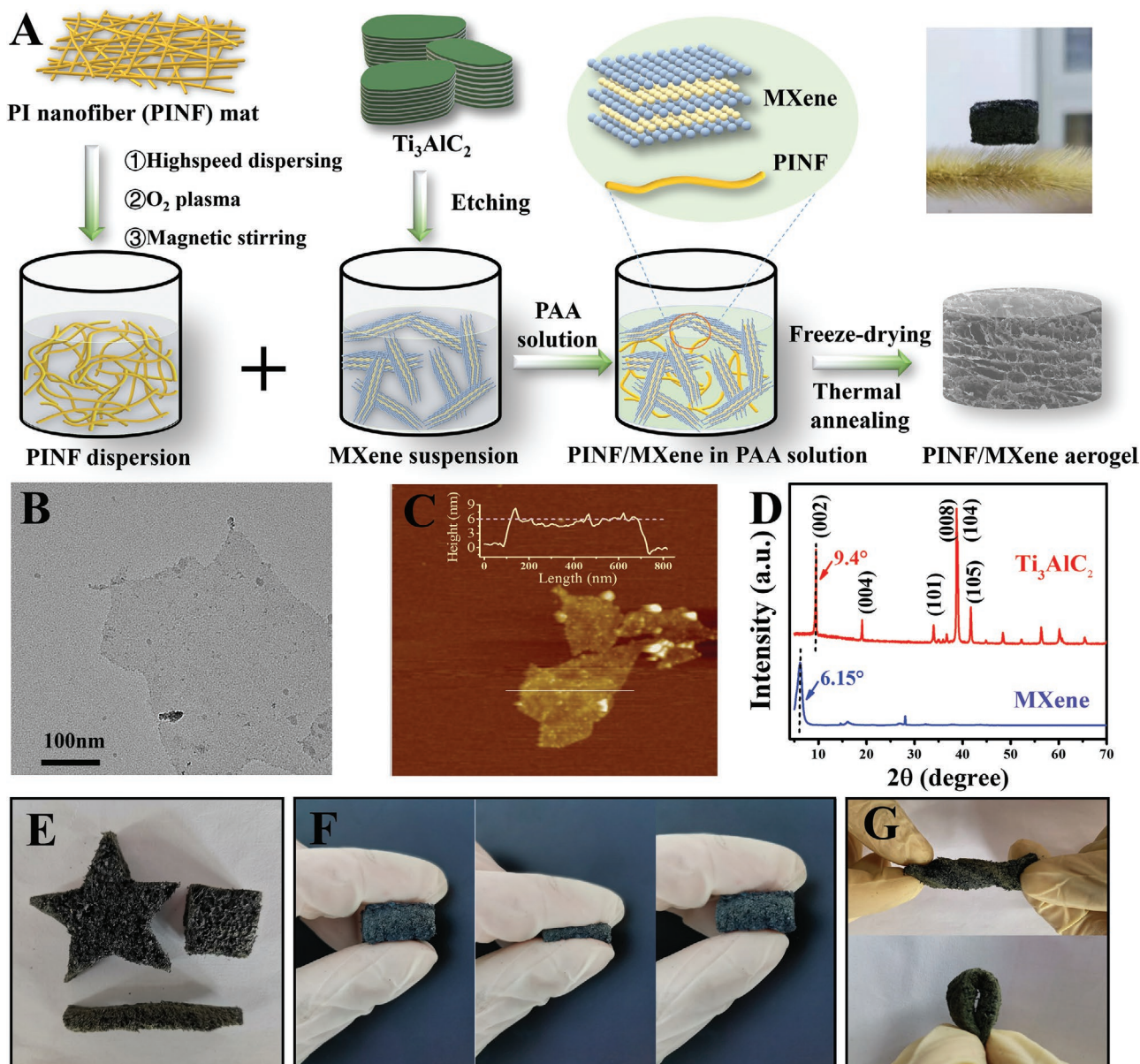
Figure 1. Preparation of PINF/MXene composite aerogel. A) Schematic diagram for the preparation process of PINF/MXene composite aerogel. B) SEM and C) AFM images of MXene. D) XRD patterns of Ti_3AlC_2 and MXene. E) Digital photos PINF/MXene composite aerogel in various shapes. Digital pictures showing the PINF/MXene composite aerogel can withstand F) high level of compression, G) twisting and bending.

the composite aerogel with excellent performances when served as the piezoresistive sensor.

The interior microstructures and morphologies of the pure PINF aerogel and PINF/MXene composite aerogel were observed using SEM. As shown in Figure 2A–C, the pure PINF aerogel exhibits an isotropic open-cellular structure with a major cellular pore size of 80–100 μm originating from the solvent crystal nucleation and phase separation between solvent crystals and the PINF, and these cell walls are composed of tangled fibers, forming numbers of minor cell pores with size of 3–5 μm. As for the PINF/MXene composite aerogel (PM-10), apart from the hierarchical open-cellular structure, the orientation of 2D MXene nanosheet occurs due to the growth and

expansion of solvent crystals, resulting a typical well-ordered layered hierarchical cellular structure, where the PINF acts as strut to connect adjacent layers and the layer spacing is about 100 μm (**Figure 2**D). Zooming in on a layer of the cellular structure reveals that the layer is composed of 2D MXene nanosheet and 1D PINF, which are strongly welded together by the thermal imidized PAA (Figure 2E). The robust bonding between PINF and MXene can effectively prevent the composite aerogel from being destructed upon larger pressure. In addition, the adjacent interlayer structure affords the composite aerogel with sufficient space for compression and the PINF strut has excellent flexibility and bendability like a spring. All these enable the composite aerogel to bear large serious
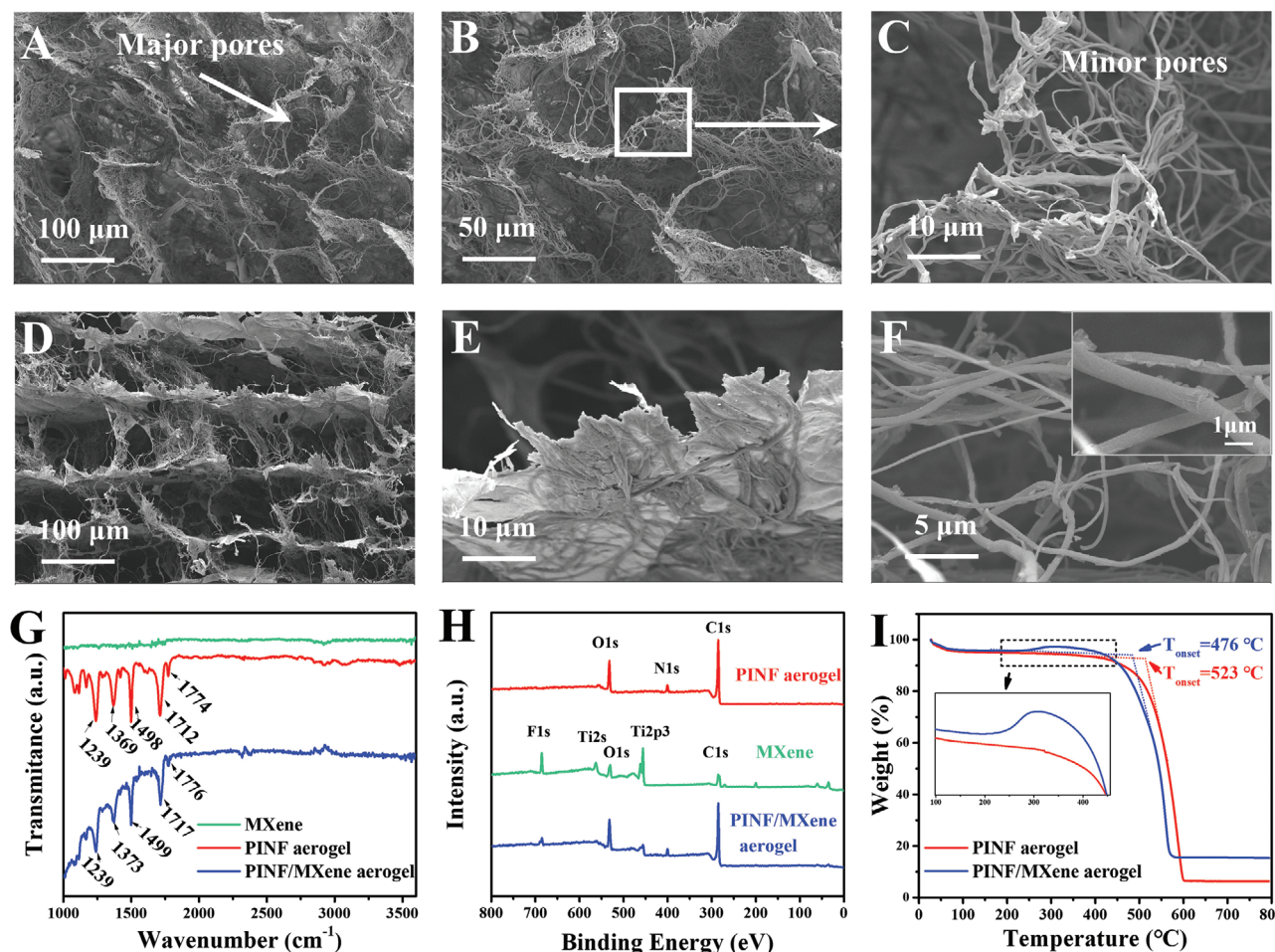
Figure 2. Morphology and structure characterizations of PINF/MXene composite aerogel. SEM images of A–C) pure PINF aerogel and D–F) PINF/MXene composite aerogel at different magnifications, the insert in (F) is the high-magnification SEM image showing the Mxene wrapped PINF. G) FT-IR spectra and H) XPS survey spectra of MXene, pure PINF aerogel, and PINF/MXene composite aerogel. I) TG curves of pure PINF aerogel and PINF/MXene composite aerogel.

compression and restore its initial shape quickly. Importantly, it can be clearly seen that the PINF in cell strut is also fully wrapped by MXene nanosheet (Figure 2F), which will undoubtedly endow the composite aerogel with excellent electrical conductivity. Therefore, the obtained PINF/MXene composite aerogel with the "layer-strut" bracing architecture possesses great potential applications for piezoresistive sensor with good stability, highly compressibility, and excellent recoverability.

The successful synthesis of PINF/MXene composite aerogel and the interfacial interaction between MXene and PI were then verified by FT-IR and XPS. Figure 2G presents the FT-IR spectra of the pure PINF aerogel and PINF/MXene composite aerogel. Clearly, the pure PINF aerogel exhibits the characteristic peaks of polyimide, including the C=O symmetric and asymmetric vibration on the imine ring at 1774 and 1712 cm^{-1}, the benzene ring C=C stretching vibration at 1498 cm^{-1}, C−N stretching vibration at 1369 cm^{-1} and C−O stretching vibration at 1239 cm^{-1}.[22] As for the PINF/MXene composite aerogel, the C=O and C−N peaks shift to higher wavelengths (1776, 1717, and 1373 cm^{-1}, respectively) compared with the pure PINF aerogel, which is mainly attributed to the formation of

hydrogen bonding between C=O and C−N groups of PAA and the functional groups of MXene sheets,[45] enabling the effective load transfer and good resistance upon compression. In addition, as shown in Figure 2H, all the typical peaks of MXene are observed from the XPS spectrum of PINF/MXene composite aerogel, but the peak intensity of C 1s and O 1s become stronger and a new N 1s peak also appears, demonstrating the existence of polyimide.[22,44] In addition, all the peaks of Ti 2p spectrum in Figure S4, Supporting Information, are almost unchanged, indicating that the thermal imidization process has no effect on MXene.[45] Moreover, thermogravimetric analysis (TGA) was conducted to evaluate the thermal stability of PINF/MXene composite aerogel in air atmosphere. As seen in Figure 2I and Figure S5, Supporting Information, the onset decomposition temperature (T_{onset}) and maximum decomposition rate temperature (T_{max}) of the composite aerogel are identified to be 476 and 560 °C, which are lower than those of pure PINF aerogel ($T_{onset} = 523$ °C, $T_{max} = 590$ °C). The degradation of the thermal stability is mainly ascribed to the excellent thermal conductivity of MXene that acts as a heat source to induce the decomposition of PI at a lower temperature. Besides, it can be
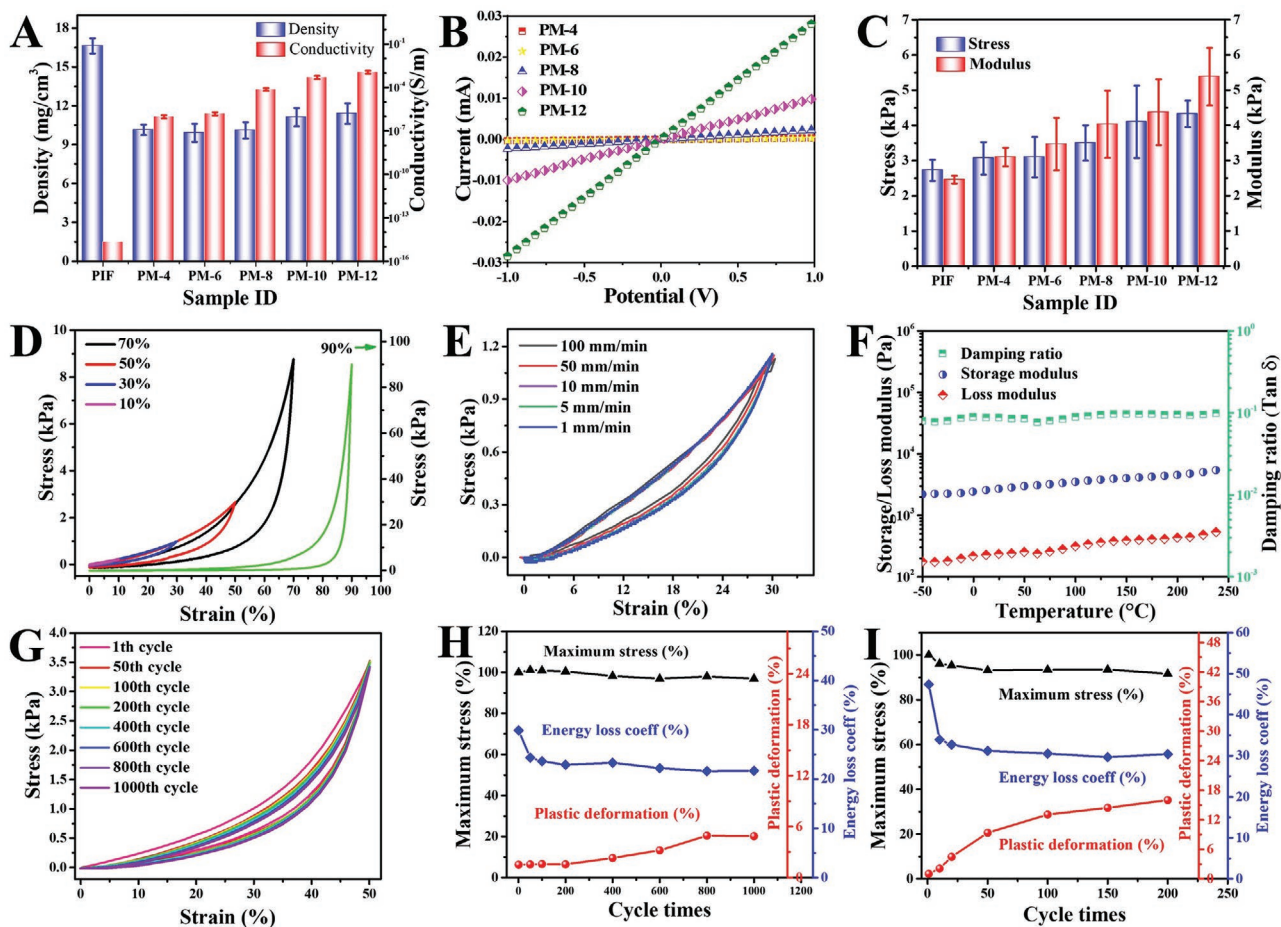
Figure 3. Mechanical and electrical properties of PINF/MXene composite aerogel. A) Bulk density and conductivity of pure PINF aerogel and PINF/MXene composite aerogel. B) I–V curves of PINF/MXene composite aerogel. C) The compression strength and modulus of pure PINF aerogel and PINF/MXene composite aerogel at 50% compression strain at a compression rate of 5 mm min^{-1}. The typical stress–strain curves of PINF/MXene composite aerogel D) at different set strains and E) at different compression rates. F) Dynamic rheological behavior of PINF/MXene composite aerogel in the temperature range from −50 to 250 °C at 1 Hz. G) Stress–strain curves and H) corresponding maximum stress, plastic deformation, and energy loss of PINF/MXene composite aerogel over 1000 cycles at 50% strain at a compression rate of 10 mm min^{-1}. I) The maximum stress, plastic deformation, and energy loss of PINF/MXene composite aerogel over 200 cycles at 80% strain.

clearly observed from the inset in Figure 2I that the curve of PINF/MXene composite aerogel exhibits an unusual upward trend at about 220 °C, which is mainly caused by the severe oxidation of MXene. As a result, it will undoubtedly affect the electrical property and piezoresistive sensing performances of composite aerogel under a higher working temperature. Nevertheless, thanks to the outstanding thermal stability of the polyimide matrix, the PINF/MXene composite aerogel still has great potential to work under broader usage temperature range than other traditional polymer-based pressure sensor, which will be further studied in the following part.

The loading of the MXene have a significant effect on the bulk density, electrical conductivity, and mechanical properties of the PIF/MXene composite aerogel. As shown in **Figure 3**A, due to the existence of MXene that prevents the shrinkage of the aerogel skeleton during the preparation process, the PM-6 composite aerogel possesses a density of 9.98 mg cm^{-3}, which is much lower than that of pure PINF aerogel (16.63 mg cm^{-3}). With the further increase of the MXene loading, the aerogel skeleton tends to be stable gradually and the density exhibits

a slight increase due to the higher MXene loading. In addition, the electrical conductivity displays a significant increase based on the construction of effective conductive networks with increasing MXene loading, and it almost reaches a stable value for PM-10 and PM-12 composite aerogels. In addition, the good linear ohmic behavior of the I–V curves demonstrates the stable electrical properties of all the prepared composite aerogels (Figure 3B), which are beneficial for stable signal output and sensing performances. Figure 3C and Figure S6, Supporting Information, show the compression properties of the pure PINF aerogel and different PINF/MXene composite aerogels at 50% strain. Obviously, the composite aerogel exhibits superior compression strength and modulus over pure PINF aerogel, and higher compression strength and modulus are obtained for the composite aerogels with higher MXene loading. All of these are mainly ascribed to the special 3D "layer-strut" bracing architecture and the good interfacial interaction between MXene and PINF, leading to the effective load transfer upon external compression. As a result, the PINF/MXene composite aerogel with tunable compression property could be achieved through

changing the MXene loading to satisfy different practical application requirements. Here, it should be noted that all the prepared aerogels possess ultralow modulus (2.49–5.37 kPa), enabling it great potential for highly sensitive piezoresistive sensor.

Subsequently, a series of compression tests under different conditions were systematically conducted to evaluate the structural stability of the PINF/MXene composite aerogel, which is crucial for high-performance piezoresistive sensor. Figure 3D presents the stress–strain curves of the PINF/MXene composite aerogel at different set strains, and excellent reversible compressibility is observed at any set strain even up to 90%, where the composite aerogel is compressed into a sheet and restores back to its initial shape quickly after releasing the external compression (Figure S7, Supporting Information), indicating the outstanding robustness and elasticity of the "layer-strut" bracing cellular structure. In addition, it is observed in Figure 3E that the PINF/MXene composite aerogel displays stable stress–strain curves at different compression rates, showing the compression rate independent mechanical properties, which is of great significance for the practical applications. Furthermore, the viscoelastic properties of the PINF/MXene composite aerogel are almost constant over a wide temperature range from −50 to 250 °C, demonstrating the excellent tolerance to both high and low temperature (Figure 3F). Besides, the extremely low damping ratio (0.1) indicates that the PINF/MXene composite aerogel has little energy loss in dynamic deformation, endowing it with outstanding elasticity.[23,46] Cyclic compression test at 50% strain was subsequently performed to further evaluate the fatigue resistance of the PINF/MXene composite aerogel in long-term compression process. As shown in Figure 3G, the maximum stress of the composite aerogel remains approximately constant over 1000 compression cycles along with a slight increase of plastic deformation from 1.55% to 4.94%. Additionally, the energy loss coefficient (the ratio of the hysteresis loop area to the area under the loading curve) displays a slight decrease trend in the first 50 cycles and then tends to be stable at 21% in the following cycles, where the stress–strain curves almost overlap each other (Figure 3H), showing the extremely small energy dissipation during cyclic compression and the excellent recoverability. After that, the micromorphology of the aerogel before and after compression over 1000 cycles at 50% strain was observed, and the special hierarchical nanofibrous cellular structure was well maintained without obvious cell structure collapse (Figure S9, Supporting Information). Meanwhile, similar results are also obtained for the composite aerogel at a larger strain up to 80% (Figure 3I; Figure S8, Supporting Information). All these indicate the excellent structural robustness, superelasticity, and fatigue resistance of the prepared PINF/MXene composite aerogel.

Here, the piezoresistive sensing performances of PINF/MXene composite aerogel were systematically investigated. **Figure 4**A displays the typical relative resistance variation ($\Delta R/R_0 = (R-R_0)/R_0$, where R and R_0 represent the instantaneous resistance and initial resistance, respectively) of the PINF/MXene composite aerogel with increasing compression strain up to 90%, in which three special sensing ranges are clearly observed. Generally, the variation of the conductive networks of CPCs upon external compression plays a critical role in the piezoresistive sensing behaviors. As shown in Figure S10,

Supporting Information, the nanofibrous cellular strut bends upon the initial external compression, causing the close stacking of adjacent cellular layers in the final compression stage. A schematic diagram as shown in Figure 4D was drawn to further understand the detail piezoresistive sensing mechanism during the whole compression process. In the initial compression strain range of 0–16%, the separated conductive fibers in cellular strut bend and contact with each other, causing the exponential decrease in resistance due to the construction of new conductive networks. With the further increase of the compression strain to 60%, it displays a rapidly linear decrease trend based on the synchronous increase of the face to face contact between adjacent cellular layers, leading to more effective conductive networks and highest sensitivity in the whole compression process. Generally, strain sensitivity of sensor is assessed by the gauge factor (GF = $(\Delta R/R_0)/\varepsilon$, where ε stands for the applied strain), which is calculated to be 1.67 within the linear strain sensing range. After that, the PINF/MXene composite aerogel goes into the densification region where the adjacent cellular layers begin to stack with each other, so the resistance exhibits slowly exponential decreasing trend and tends to be stable. Meanwhile, the relative resistance variation of PINF/MXene composite aerogel versus pressure was also plotted based on the stress–strain curves (Figure S11, Supporting Information). As seen in Figure 4B, a sharp decrease in resistance is observed in the initial pressure range of 0–5 kPa and the pressure sensitivity (S, $S = (\Delta R/R_0)/P$, where P is the applied pressure) is identified to be 0.14 kPa^{-1}, which is superior to other reported works.[34,47–49] This can be mainly ascribed to the low modulus of the composite aerogel that enables the significant variation of the conductive networks upon small pressure, including the point–point contact between adjacent conductive fibers in cellular strut and the face to face contact between adjacent cellular layers. Subsequently, the sensing curve gradually flattens out due to the densification of the composite aerogel, and the sensitivity in the pressure range of 40–85 kPa decreases to 0.002 kPa^{-1}. Figure 4C displays the stepwise piezoresistive sensing behavior of the PINF/MXene composite aerogel up to 90% strain. Clearly, the maximum relative resistance variation increases with the compression strain levels and the resistance can recover to its initial value after the release of external compression, showing the good recognition toward various compression strain levels and good recoverability. Besides, the I–V curves of the original, compressed, and released states of PINF/MXene composite aerogel were studied (Figure S12, Supporting Information). The increased slop of the curve upon 50% compression strain indicates the reduced resistance, which is consent with the results shown in Figure 4A. In addition, the I–V curve in the released state is almost coincided with that in the initial state, further confirming the good compression recoverability of the composite aerogel.

The cyclic piezoresistive sensing performances of the PINF/MXene composite aerogel under different strain/pressure levels were explored as well. As depicted in Figure 4E,F, the PINF/MXene composite aerogel exhibits outstanding cyclic stability and reproductivity for every stage, especially at 90% strain per 85.21 kPa. Notably, a small pressure as low as 0.01 kPa at 0.5% compression strain can also be accurately detected. All these indicate the PINF/MXene composite aerogel can be
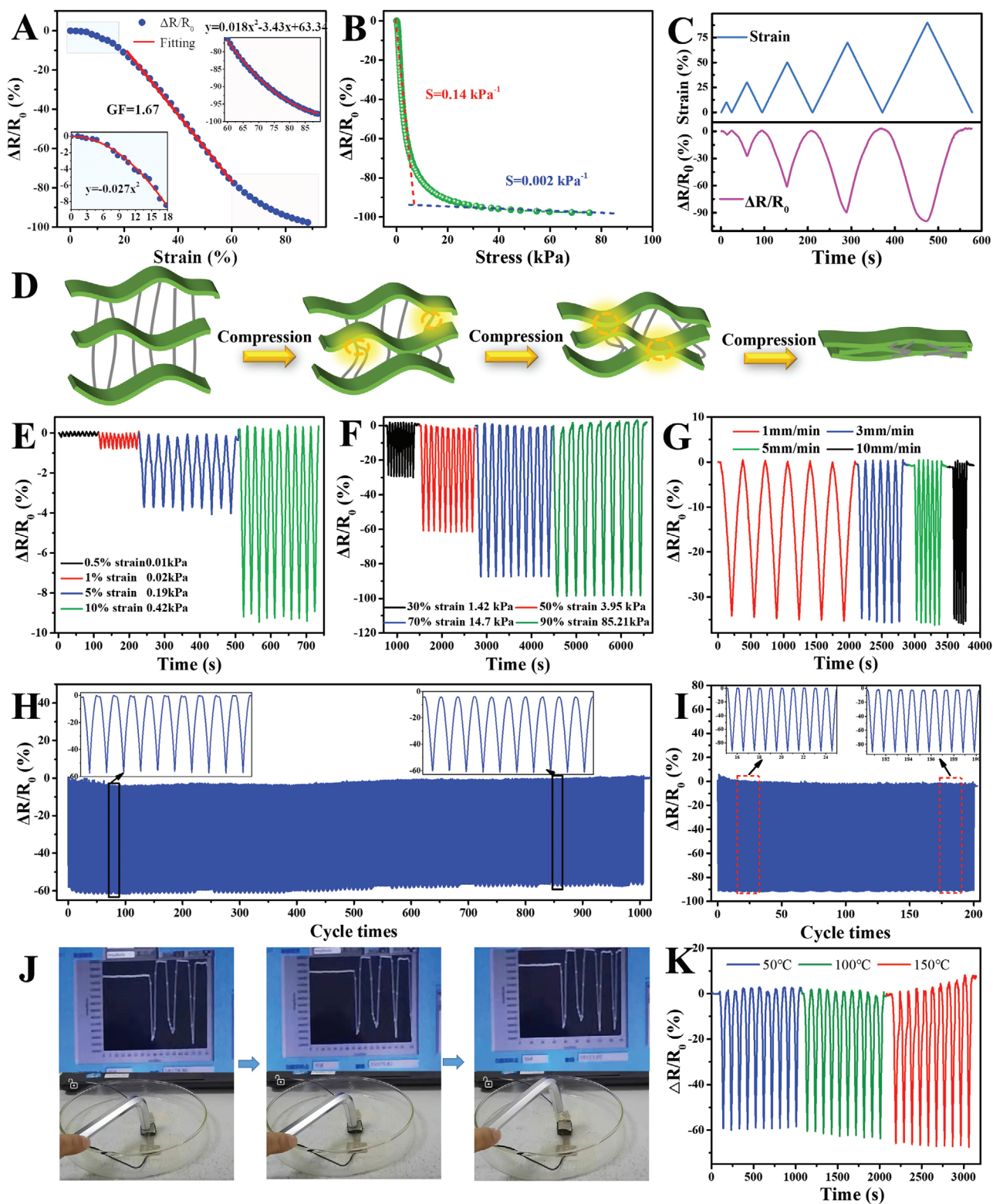
Figure 4. Piezoresistive sensing performances of PINF/MXene composite aerogel. $\Delta R/R_0$ of PINF/MXene composite aerogel as a function of A) compression strain and B) pressure. C) Stepwise piezoresistive sensing behavior of PINF/MXene composite aerogel up to 90% strain. D) Schematic diagram of the piezoresistive sensing mechanism of PINF/MXene composite aerogel. Cyclic piezoresistive sensing performances of PINF/MXene composite aerogel E,F) under different compression strain/pressure levels at a compression rate of 5 mm min^{-1} and G) at different compression rates at 50% strain. Cyclic piezoresistive sensing performances of PINF/MXene composite aerogel at H) 50% strain over 1000 cycles and I) 80% strain over 200 cycles. Piezoresistive sensing performance of PINF/MXene composite aerogel under J) ultralow temperature and K) high temperature environments.

applied for detecting both tiny and high external strain/pressure. Moreover, as depicted in Figure 4G, stable cyclic sensing behavior of the composite aerogel under different compression rates further demonstrates that the compression rate has no effect on the piezoresistive sensing performance, which is consistent with the compression rate independent mechanical property shown in Figure 3E. The response time of the pressure sensor is also an important index to evaluate the sensing performance. Under an instantaneous strain of 1%, it exhibits fast response time of 220 ms and recovery time of 140 ms (Figure S13, Supporting Information). Generally, as mentioned in Table S1, Supporting Information, our PINF/MXene aerogel possesses superior sensing performance compared with other reported works. Furthermore, the long-term cyclic compression was also conducted to verify the fatigue resistance of the pressure sensor. Obviously, the PINF/MXene composite aerogel presents excellent stability and recoverability over 1000 cycles at 50% strain (Figure 4H) and 200 cycles at 80% strain (Figure 4I), showing the outstanding fatigue resistance and piezoresistive sensing stability. More importantly, due to the excellent physical property of PI matrix, the composite aerogel exhibits a stable piezoresistive sensing ability even in extremely harsh environments such as the liquid nitrogen (Figure 4J and Video S2, Supporting Information) and the high temperature of 50, 100, and 150 °C (Figure 4K). But the unstable sensing behavior occurs at higher temperature of 200 °C (Figure S14, Supporting Information), which is induced by the oxidation of MXene (see the TG results in Figure 2I) that destroy the electrical property of the composite aerogel. But it should be noted that it still displays broader usage temperature range than other traditional polymer-based pressure sensors which is limited by the thermal stability of the polymer matrix. Meanwhile,

high temperature resistant carbon fillers (such as carbon black, carbon nanotubes, and graphene, etc.) can be used instead of MXene for preparation of high temperature resistant PI based piezoresistive sensor, and it has been verified in Figure S15, Supporting Information, that the PI/CNT composite aerogel possesses outstanding piezoresistive sensing stability and reproductivity under 200 °C.

To demonstrate the promising potential of the PINF/MXene composite aerogel for full range piezoresistive sensing detection, it was assembled into a piezoresistive sensor and attached to different human body parts using a common adhesive tape to detect a series of human bodily motion and human physical signals. As seen in **Figure 5**A, a carotid pulse rate of 65 beats per min can be accurately detected by the sensor attached to volunteer's cervical artery, and the three faint characteristic peaks of human pulse, which are corresponded to the percussion wave (P), tidal wave (T), and diastolic wave (D), can also be clearly identified. Besides, the sensor fixed onto the mask outputs stable and regular signal upon the inhalation and exhalation of volunteer (Figure 5B), which is caused by the generated airflow that exert certain compression on the sensor, providing a facile, low-cost, and efficient method for long-time respiration monitoring. Hence, the sensor has great potential for real-time human health monitoring. Additionally, based on the compression effect caused by the vibration of the vocal cords, pronunciation can also be clearly identified when the sensor is attached to the throat. As shown in Figure 5C, three typical sensing peaks corresponding to the three syllables of word of "sensor" is accurately detected, demonstrating the feasibility of the sensor for the fabrication of voice recognition devices. Meanwhile, it can also accurately capture the frequency of head shaking (Figure 5D). As for the human body motion detection, it can be
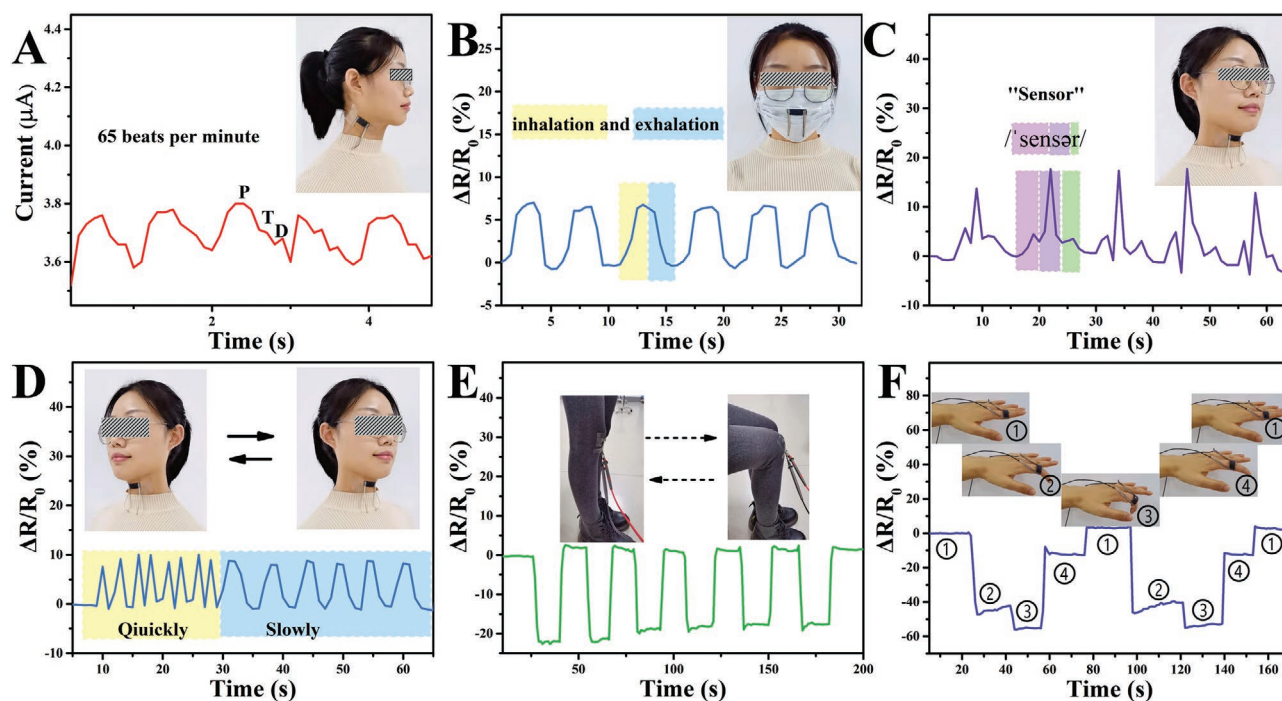

Figure 5. Sensing performances of the PINF/MXene composite aerogel served as a pressure sensor for the real-time detection of A) carotid pulse, B) inhalation and exhalation, C) pronunciation, D) head shaking, E) knee bending, and F) finger bending.
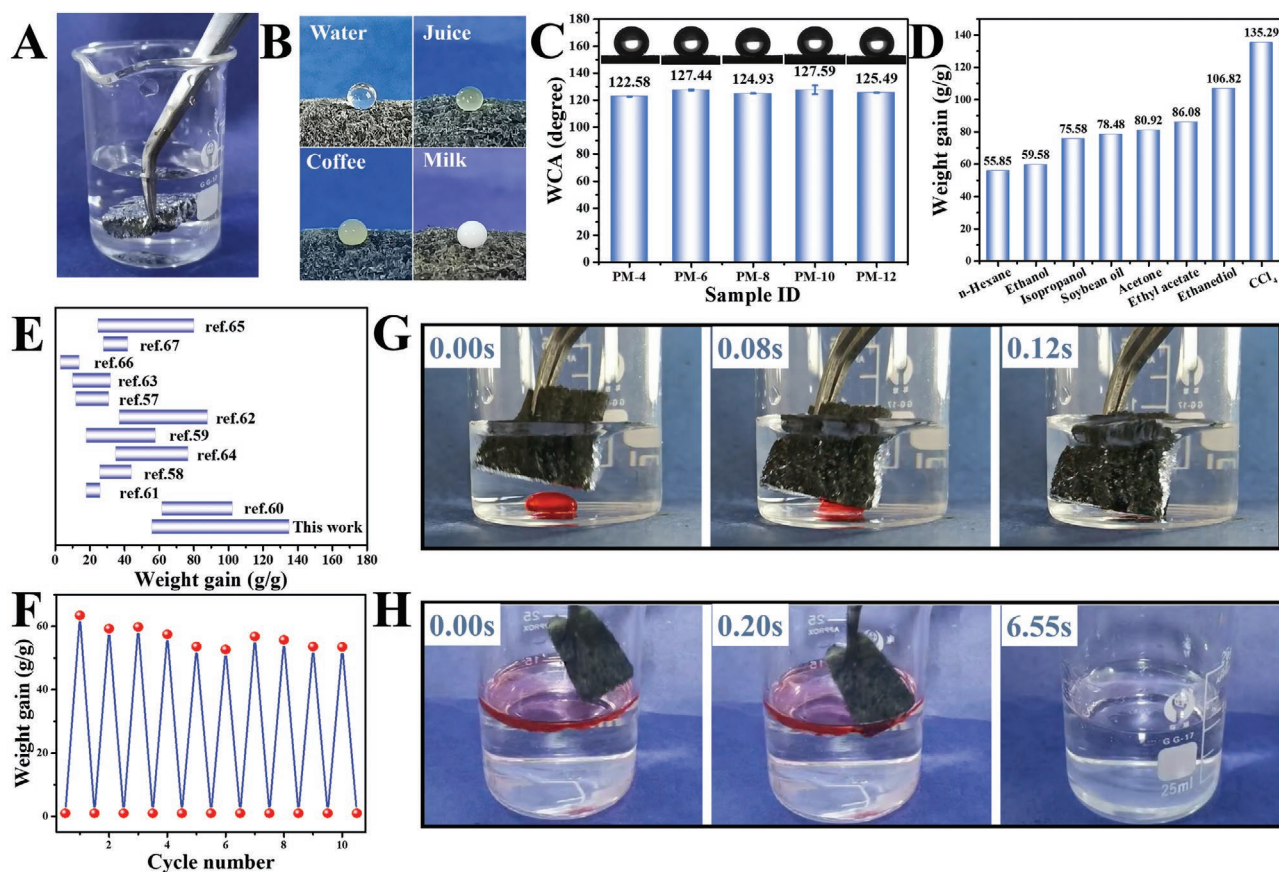
**ADVANCED
SCIENCE NEWS**
www.advancedsciencenews.com

**ADVANCED
FUNCTIONAL
MATERIALS**
www.afm-journal.de

Figure 6. Digital pictures showing A) the PINF/MXene composite aerogel immersed in water and B) the state of different liquid droplets on the surface of PINF/MXene composite aerogel. C) The water contact angle (WCA) of different PINF/MXene composite aerogels. D) Adsorption capacity of PINF/MXene composite aerogel for various oils and organic solvents. E) Comparison of the adsorption capacity of our composite aerogel with other previously published works. F) Cyclic adsorption property of the PINF/MXene composite aerogel for ethanol. Digital pictures showing the absorption of G) carbon tetrachloride from the bottom of water and H) soybean oil from the surface of water using the PINF/MXene composite aerogel.

clearly observed in Figure 5E,F that the sensor exhibits stable and reproducible sensing signal toward repetitive knee bending and good recognition to different finger bending angles. As a conclusion, our prepared PI/MXene composite aerogel based piezoresistive sensor possesses great potential application for wearable electronic devices

Recently, the investigations on functional aerogels have aroused great interests due to their special micro structure.[50–55] Here, based on the low density and porous structure of the prepared PINF/MXene composite aerogel, its wettability was then systematically investigated to disclose its application for oil/water separation. Clearly, as shown in **Figure 6**A and Video S3, Supporting Information, the surface of the composite aerogel immersed in water displays strong light reflection, which is caused by the trapped air layer that lead to the total light reflection, preventing it from being wetted effectively.[18] In addition, various liquid droplets, including water, juice, coffee, and milk, can remain sphere shape on the composite aerogel surface, showing the hydrophobicity of the composite aerogel (Figure 6B). Water contact angle (WCA) measurement was then conducted and shown in Figure 6C. Owing to the rough surface structure and the hydrophobicity of PI matrix, the WCA values of all PINF/MXene composite

aerogel are all about 125°, showing the naturally superior hydrophobicity even without the need of any additional surface treatment. Combined with low density and porous structure, the prepared PINF/MXene composite aerogel possesses great potential application for oil/water separation. Figure 6D illustrates the adsorption capacity of the PINF/MXene composite aerogel for various oils and organic solvents, including *n*-hexane, ethanol, isopropanol, soybean oil, acetone, ethyl acetate, ethanediol, and CCl_4. During the test, the composite aerogel is immersed into oil or organic solvent for 30 min and then taken out followed by wiping the excess oil or solvent using filler paper. In addition, the weight gain (weight ratio of the composite aerogel after and before absorption) is applied to evaluate the adsorption capacity of the composite aerogel. Clearly, the absorption capacity is highly dependent on the density and viscosity of liquids, and the weight gain of the composite aerogel ranges from 55.85 to 135.29 times weight of dried samples. As a result, our composite aerogel presents much higher adsorption capacity compared with other previously reported oil/water separation materials (Figure 6E) such as poly(lactic acid) foam (12–31 times),[56] graphene/ polyurethane sponges (25.8–44.1 times),[57] polyimide/MXene aerogels (18–58 times),[58] etc.[59–66]

**ADVANCED
SCIENCE NEWS**

www.advancedsciencenews.com

**ADVANCED
FUNCTIONAL
MATERIALS**

www.afm-journal.de

Subsequently, the cyclic adsorption property of the PINF/MXene composite aerogel for ethanol was further explored using the squeezing approach to evaluate its recyclability. As shown in Figure 6F, the adsorption capacity first displays a slight decrease trend due to the adjustment of the porous structure during cyclic compression process, but it quickly turns to be stable in the following repetitions and all the absorbed ethanol can be completely squeezed out in each cycle, showing excellent structure stability of the composite aerogel. In view of the excellent absorption capacity of the composite aerogel, oil–water separation experiments were performed. In Figure 6G,H and Videos S4 and S5, Supporting Information, the composite aerogel can completely absorb a drop of red carbon tetrachloride from the bottom of the water in a very short time of 0.12 s without water absorption. Additionally, the diffused soybean oil on surface of water can also be well absorbed within 6.55 s. All of the results above verify the prepared PI/MXene composite aerogel is also an ideal decontamination material in applications of environmental protection.

3. Conclusions

In summary, we have designed and developed a multifunctional conductive PINF/MXene composite aerogel with typical "layer-strut" bracing porous architecture through a simple freeze-drying and thermal imidization process. Due to the special porous architecture and the robust bonding between PINF and MXene, the resulting composite aerogel exhibits ultralow density, intriguing temperature tolerance, superior compressibility/recoverability, and excellent fatigue resistance. All these endow it to be served as ideal piezoresistive sensor with good sensing capacity up to 90% compression strain (corresponding 85.21 kPa), an ultralow detection limit of 0.5% compression strain (corresponding 0.01 kPa), good fatigue resistance over 1000 cycles, outstanding piezoresistive sensing stability and reproductivity in extremely harsh environments such as the liquid nitrogen and the high temperature of 50, 100, and 150 °C. More importantly, the composite aerogel based piezoresistive sensor has also shown good performance in human bodily motion and physical signals detection. Furthermore, we also demonstrate that the composite aerogel is a superior high-efficient oil/water separation material compared with the recently reported works. We believe that this study can supply a simple but effective strategy for fabricating high-performance multifunctional platform.

4. Experimental Section

Materials and Chemicals: 4,4′-Diaminodiphenyl ether (ODA, 98%), 3,3′,4,4′-biphenyltetracarboxylic dianhydride (BPDA, 97%), and lithium fluoride (LiF) were purchased from Aladdin Reagent Co., Ltd (China). *N*-methyl-2-pyrrolidone (NMP, AR) was obtained from Tianjin Kemiou Chemical Reagent Co. Ltd (China). Triethylamine (TEA, 99.0%) was provided by Tianjin Damao Chemical Reagent Factory (China). Hydrochloric acid (HCl) was obtained from Luoyang Haohua Chemical Reagent Co. Ltd (China). Titanium aluminum carbide (Ti₃AlC₂, 400 mesh) was bought from Jilin 11 Technology Co. Ltd (China). Electrospun PINF mat (fiber diameter: ≈400 nm, Figure S16, Supporting Information) were supplied by Jiangxi Xiancai Nanofibers Technology Co., Ltd (China). All of the materials and chemicals were used as received without any treatment.

Preparation of Ti_3C_2X MXene Nanosheets: Ti_3C_2X MXene nanosheets was prepared by selectively etching the Al layer of Ti_3AlC_2 with HCl and LiF as described in previous publications.[67,68] Typically, 2.0 g of Ti_3AlC_2 was slowly added to the mixture containing 2.0 g LiF and 40 mL HCl (9 M) in a 100 mL Teflon beaker, which was stirred gently at 35 °C for 24 h for the etching of Al. The obtained products were washed with deionized water and centrifuged at 5000 rpm for several times until the pH value of the supernatant was above 5. Then, the sediment was dispersed in anhydrous ethanol and treated in an ultrasonic bath (180 W) for 60 min to delaminate the MXene flakes, which was followed by the centrifugation at 10 000 rpm for 10 min to remove the ethanol. Finally, the exfoliated mixture was re-dispersed in deionized water and the impurities were eliminated by centrifuged at 3500 rpm for 3 min for multiple times and the dark green supernatant was collected as MXene suspension (1 mg mL⁻¹).

Preparation of PINF/MXene Composite Aerogels: A typical procedure for the preparation of the PINF/MXene composite aerogels mainly includes the following three steps: i) 150 mg PINF mat was first cut into small pieces (5 × 5 mm²) and soaked in 30 mL dioxane for 12 h, which was smashed using high-shear homogenizer (FJ200-SH) at a shear rate of 13 000 rpm for 30 min to obtain PINF suspension. Then, PINF was freeze-dried and further treated with oxygen plasma for 8 min to improve its hydrophilicity. Specifically, the freeze-dried PINF was spread in a large petri dish and sealed with an ultrathin gauze to prevent the fiber from flying out during the oxygen plasma treatment process. To ensure the homogeneous treatment of the fiber surface, PINF was flipped using tweezers for three times. ii) 150 mg oxygen plasma treated PINF and 8.3 mL MXene suspension was added to 20.7 mL deionized water and magnetically stirred for 30 min. Poly (amic acid)-triethylamine salt (PAA-TEA) solution (1 mL, 50 mg mL⁻¹), which was prepared according to the authors' previous work,[19] was then added as adhesion agent under magnetic stirring for 30 min to obtain homogeneous PINF/MXene dispersion. Afterward, the mixture was transferred to glass culture dishes and frozen in a refrigerator (−20 °C) for 12 h and then dried in a lyophilizer (−85 °C, 8 Pa) for 72 h to obtain PAA-welded PINF/MXene aerogel. iii) The obtained PAA-welded PINF/MXene aerogel was transferred to a tube furnace and thermally imidized by stepwise heating to 150 °C (3 °C min⁻¹) and 350 °C (1.5 °C min⁻¹) in N₂ atmosphere. A series of PINF/MXene aerogels with different compositions were prepared according to the formulations listed in Table S2, Supporting Information. In this work, the as-prepared composite aerogels were named as PM-*x*, where *x* represents the weight percentage of MXene in the composite aerogels. In addition, pure PINF aerogel was also fabricated using the same procedure without the addition MXene.

Characterizations: The morphology and size of MXene was observed using transmission electron microscope (JEOL JEM-2100F) and atomic force microscope (AFM, MFP-3D Origin+ / icon). XRD was performed by X-ray diffraction spectrometer (Ultima IV). Scanning electron microscopy (SEM) were conducted with a JEOL JSM-7500F at an accelerating voltage of 5 kV. Fourier transform infrared (FTIR) spectrum in the 600–4000 cm⁻¹ was recorded on the Nicolet Nexus 870 instrument by the attenuated total reflection mode. X-ray photoelectron spectroscopy (XPS) was measured by an X-ray photoelectron spectrometer (Thermo ESCALAB 250XI) with an excitation source of Al Kα radiation. TGA was performed on a thermogravimetric analyzer (NETZSCH STA 449 F5 Jupiter) from room temperature to 1000 °C at a heating rate of 10 °C min⁻¹ under air atmosphere. Dynamic mechanical analysis was performed by a dynamic mechanical analyzer (TA Q800) from −50 to 250 °C at a heating rate of 5 °C min⁻¹ under a set frequency of 1 Hz and a fixed oscillatory strain of 2%. The density of the composite aerogels was calculated by dividing the mass by the corresponding volume. Compression tests were conducted using a universal testing machine (UTM2203) equipped with 100 N load cells. For the electrical property and piezoresistive sensing performance tests, flexible conductive tapes were adhered onto two opposite surfaces of cube composite aerogel and conductive silver paste was applied to

enhance the adhesion strength between them. Volume resistance (R) of composite aerogels was tested using digit precision multimeter (Tektronix DMM4050), the corresponding volume conductivity (σ) was calculated using the following formula: $\sigma = H/(RA)$, where H and A are height and cross-section area of composite aerogels, respectively. I–V curves and response time were measured by an electrochemical workstation (RST5200F) coupled with a universal testing machine. The piezoresistive sensing performance of composite aerogels was tested using the digit precision multimeter and the universal testing machine together. In this paper, PM-10 composite aerogel was selected for all tests unless noted otherwise.

Supporting Information

Supporting Information is available from the Wiley Online Library or from the author.

Conflict of Interest

The authors declare no conflict of interest.

[1] W. Zhai, Q. Xia, K. Zhou, X. Yue, M. Ren, G. Zheng, K. Dai, C. Liu, C. Shen, *Chem. Eng. J.* **2019**, *372*, 373.

[2] Q. Li, R. Yin, D. Zhang, H. Liu, X. Chen, Y. Zheng, Z. Guo, C. Liu, C. Shen, *J. Mater. Chem. A* **2020**, *8*, 21131.

[3] Y. Zheng, Y. Li, Y. Zhou, K. Dai, G. Zheng, B. Zhang, C. Liu, C. Shen, *ACS Appl. Mater. Interfaces* **2020**, *12*, 1474.

[4] S. Zhang, H. Liu, S. Yang, X. Shi, D. Zhang, C. Shan, L. Mi, C. Liu, C. Shen, Z. Guo, *ACS Appl. Mater. Interfaces* **2019**, *11*, 10922.

[5] Z. Li, M. Zhu, J. Shen, Q. Qiu, J. Yu, B. Ding, *Adv. Funct. Mater.* **2019**, *30*, 1908411.

[6] Z. Liu, Y. Ma, H. Ouyang, B. Shi, N. Li, D. Jiang, F. Xie, D. Qu, Y. Zou, Y. Huang, H. Li, C. Zhao, P. Tan, M. Yu, Y. Fan, H. Zhang, Z. L. Wang, Z. Li, *Adv. Funct. Mater.* **2019**, *29*, 1807560.

[7] B. Nie, R. Huang, T. Yao, Y. Zhang, Y. Miao, C. Liu, J. Liu, X. Chen, *Adv. Funct. Mater.* **2019**, *29*, 1808786.

[8] R. Yu, C. Pan, J. Chen, G. Zhu, Z. L. Wang, *Adv. Funct. Mater.* **2013**, *23*, 5868.

[9] S. Gong, W. Schwalb, Y. Wang, Y. Chen, Y. Tang, J. Si, B. Shirinzadeh, W. Cheng, *Nat. Commun.* **2014**, *5*, 3132.

[10] Y. J. Park, B. K. Sharma, S. M. Shinde, M. S. Kim, B. Jang, J. H. Kim, J. H. Ahn, *ACS Nano* **2019**, *13*, 3023.

[11] H. Liu, Q. Li, S. Zhang, R. Yin, X. Liu, Y. He, K. Dai, C. Shan, J. Guo, C. Liu, C. Shen, X. Wang, N. Wang, Z. Wang, R. Wei, Z. Guo, *J. Mater. Chem. C* **2018**, *6*, 12121.

[12] H. Liu, W. Huang, J. Gao, K. Dai, G. Zheng, C. Liu, C. Shen, X. Yan, J. Guo, Z. Guo, *Appl. Phys. Lett.* **2016**, *108*, 5.

[13] R. Y. Tay, H. Li, J. Lin, H. Wang, J. S. K. Lim, S. Chen, W. L. Leong, S. H. Tsang, E. H. T. Teo, *Adv. Funct. Mater.* **2020**, *30*, 1909604.

[14] L. Persano, C. Dagdeviren, Y. Su, Y. Zhang, S. Girardo, D. Pisignano, Y. Huang, J. A. Rogers, *Nat. Commun.* **2013**, *4*, 1633.

[15] H. Liu, J. Gao, W. Huang, K. Dai, G. Zheng, C. Liu, C. Shen, X. Yan, J. Guo, Z. Guo, *Nanoscale* **2016**, *8*, 12977.

[16] H. Liu, Y. Li, K. Dai, G. Zheng, C. Liu, C. Shen, X. Yan, J. Guo, Z. Guo, *J. Mater. Chem. C* **2016**, *4*, 157.

[17] H. Liu, M. Dong, W. Huang, J. Gao, K. Dai, J. Guo, G. Zheng, C. Liu, C. Shen, Z. Guo, *J. Mater. Chem. C* **2017**, *5*, 73.

[18] H. Liu, Q. Li, Y. Bu, N. Zhang, C. Wang, C. Pan, L. Mi, Z. Guo, C. Liu, C. Shen, *Nano Energy* **2019**, *66*, 104143.

[19] X. Chen, H. Liu, Y. Zheng, Y. Zhai, X. Liu, C. Liu, L. Mi, Z. Guo, C. Shen, *ACS Appl. Mater. Interfaces* **2019**, *11*, 42594.

[20] M. Wang, I. V. Anoshkin, A. G. Nasibulin, J. T. Korhonen, J. Seitsonen, J. Pere, E. I. Kauppinen, R. H. Ras, O. Ikkala, *Adv. Mater.* **2013**, *25*, 2428.

[21] H. B. Yao, J. Ge, C. F. Wang, X. Wang, W. Hu, Z. J. Zheng, Y. Ni, S. H. Yu, *Adv. Mater.* **2013**, *25*, 6692.

[22] Y. Qin, Q. Peng, Y. Ding, Z. Lin, C. Wang, Y. Li, F. Xu, J. Li, Y. Yuan, X. He, Y. Li, *ACS Nano* **2015**, *9*, 8933.

[23] Y. Si, X. Wang, C. Yan, L. Yang, J. Yu, B. Ding, *Adv. Mater.* **2016**, *28*, 9512.

[24] Z. Chen, Y. Hu, H. Zhuo, L. Liu, S. Jing, L. Zhong, X. Peng, R.-c. Sun, *Chem. Mater.* **2019**, *31*, 3301.

[25] S. Zhang, K. Sun, H. Liu, X. Chen, Y. Zheng, X. Shi, D. Zhang, L. Mi, C. Liu, C. Shen, *Chem. Eng. J.* **2020**, *387*, 124045.

[26] J. Huang, J. Wang, Z. Yang, S. Yang, *ACS Appl. Mater. Interfaces* **2018**, *10*, 8180.

[27] J. Yang, Y. Ye, X. Li, X. Lü, R. Chen, *Compos. Sci. Technol.* **2018**, *164*, 187.

[28] S. Jiang, S. Agarwal, A. Greiner, *Angew. Chem., Int. Ed. Engl.* **2017**, *56*, 15520.

[29] X. Cao, J. Zhang, S. Chen, R. J. Varley, K. Pan, *Adv. Funct. Mater.* **2020**, *30*, 2003618.

[30] Z. Qian, Z. Wang, Y. Chen, S. Tong, M. Ge, N. Zhao, J. Xu, *J. Mater. Chem. A* **2018**, *6*, 828.

[31] Y. Si, J. Yu, X. Tang, J. Ge, B. Ding, *Nat. Commun.* **2014**, *5*, 5802.

[32] I. Gouzman, E. Grossman, R. Verker, N. Atar, A. Bolker, N. Eliaz, *Adv. Mater.* **2019**, *31*, 1807738.

[33] D.-J. Liaw, K.-L. Wang, Y.-C. Huang, K.-R. Lee, J.-Y. Lai, C.-S. Ha, *Prog. Polym. Sci.* **2012**, *37*, 907.

[34] X. Zhao, W. Wang, Z. Wang, J. Wang, T. Huang, J. Dong, Q. Zhang, *Chem. Eng. J.* **2020**, *395*, 125115.

[35] M. Q. Zhao, X. Xie, C. E. Ren, T. Makaryan, B. Anasori, G. Wang, Y. Gogotsi, *Adv. Mater.* **2017**, *29*, 1702410.

[36] M. Naguib, O. Mashtalir, J. Carle, V. Presser, J. Lu, L. Hultman, Y. Gogotsi, M. W. Barsoum, *ACS Nano* **2012**, *6*, 1322.

[37] M. R. Lukatskaya, O. Mashtalir, C. E. Ren, Y. Dall'Agnese, P. Rozier, P. L. Taberna, M. Naguib, P. Simon, M. W. Barsoum, Y. Gogotsi, *Science* **2013**, *341*, 1502.

[38] M. Naguib, V. N. Mochalin, M. W. Barsoum, Y. Gogotsi, *Adv. Mater.* **2014**, *26*, 992.

[39] F. Xie, F. Jia, L. Zhuo, Z. Lu, L. Si, J. Huang, M. Zhang, Q. Ma, *Nanoscale* **2019**, *11*, 23382.

[40] L. Wang, H. Qiu, P. Song, Y. Zhang, Y. Lu, C. Liang, J. Kong, L. Chen, J. Gu, *Composites, Part A* **2019**, *123*, 293.

[41] Y. Yue, N. Liu, W. Liu, M. Li, Y. Ma, C. Luo, S. Wang, J. Rao, X. Hu, J. Su, Z. Zhang, Q. Huang, Y. Gao, *Nano Energy* **2018**, *50*, 79.

[42] R. Bian, G. He, W. Zhi, S. Xiang, T. Wang, D. Cai, *J. Mater. Chem. C* **2019**, *7*, 474.

[43] Y. Li, X. Tian, S. P. Gao, L. Jing, K. Li, H. Yang, F. Fu, J. Y. Lee, Y. X. Guo, J. S. Ho, P. Y. Chen, *Adv. Funct. Mater.* **2019**, *30*, 1907451.

[44] Z. Fan, D. Wang, Y. Yuan, Y. Wang, Z. Cheng, Y. Liu, Z. Xie, *Chem. Eng. J.* **2020**, *381*, 122696.

[45] J. Liu, H. B. Zhang, X. Xie, R. Yang, Z. Liu, Y. Liu, Z. Z. Yu, *Small* **2018**, *14*, 1802479.

[46] Z. L. Yu, B. Qin, Z. Y. Ma, J. Huang, S. C. Li, H. Y. Zhao, H. Li, Y. B. Zhu, H. A. Wu, S. H. Yu, *Adv. Mater.* **2019**, *31*, 1900651.

[47] S. Jung, J. H. Kim, J. Kim, S. Choi, J. Lee, I. Park, T. Hyeon, D. H. Kim, *Adv. Mater.* **2014**, *26*, 4825.

[48] X. Wu, Y. Han, X. Zhang, Z. Zhou, C. Lu, *Adv. Funct. Mater.* **2016**, *26*, 6246.

[49] Y. Tang, S. Gong, Y. Chen, L. W. Yap, W. Cheng, *ACS Nano* **2014**, *8*, 5707.

[50] S. Zhao, H. B. Zhang, J. Q. Luo, Q. W. Wang, B. Xu, S. Hong, Z. Z. Yu, *ACS Nano* **2018**, *12*, 11193.

[51] J. Liu, H. B. Zhang, R. Sun, Y. Liu, Z. Liu, A. Zhou, Z. Z. Yu, *Adv. Mater.* **2017**, *29*, 1702367.

[52] J. Zheng, X. Pan, X. Huang, D. Xiong, Y. Shang, X. Li, N. Wang, W.-M. Lau, H. Y. Yang, *Chem. Eng. J.* **2020**, *396*, 125197.

[53] L. Bi, Z. Yang, L. Chen, Z. Wu, C. Ye, *J. Mater. Chem. A* **2020**, *8*, 20030.

[54] J. Song, X. Guo, J. Zhang, Y. Chen, C. Zhang, L. Luo, F. Wang, G. Wang, *J. Mater. Chem. A* **2019**, *7*, 6507.

[55] Y. Tang, K. L. Yeo, Y. Chen, L. W. Yap, W. Xiong, W. Cheng, *J. Mater. Chem. A* **2013**, *1*, 6723.

[56] X. Wang, Y. Pan, X. Liu, H. Liu, N. Li, C. Liu, D. W. Schubert, C. Shen, *ACS Appl. Mater. Interfaces* **2019**, *11*, 14362.

[57] S. Zhou, G. Hao, X. Zhou, W. Jiang, T. Wang, N. Zhang, L. Yu, *Chem. Eng. J.* **2016**, *302*, 155.

[58] N. N. Wang, H. Wang, Y. Y. Wang, Y. H. Wei, J. Y. Si, A. C. Y. Yuen, J. S. Xie, B. Yu, S. E. Zhu, H. D. Lu, W. Yang, Q. N. Chan, G. H. Yeoh, *ACS Appl. Mater. Interfaces* **2019**, *11*, 40512.

[59] N. Chen, Q. Pan, *ACS Nano* **2013**, *7*, 6875.

[60] Q. Zhu, Q. Pan, *ACS Nano* **2014**, *8*, 1402.

[61] E.-C. Cho, C.-W. Chang-Jian, Y.-S. Hsiao, K.-C. Lee, J.-H. Huang, *J. Taiwan Inst. Chem. Eng.* **2016**, *67*, 476.

[62] X. Wang, Y. Pan, C. Shen, C. Liu, X. Liu, *Macromol. Rapid. Commun.* **2018**, *39*, 1800635.

[63] O. Guselnikova, A. Barras, A. Addad, E. Sviridova, S. Szunerits, P. Postnikov, R. Boukherroub, *Sep. Purif. Technol.* **2020**, *240*, 116627.

[64] A. Jamsaz, E. K. Goharshadi, *J. Mol. Liq.* **2020**, *307*, 112979.

[65] L. Zou, A. D. Phule, Y. Sun, T. Y. Zhu, S. Wen, Z. X. Zhang, *Polym. Test.* **2020**, *85*, 106451.

[66] A. Jamsaz, E. K. Goharshadi, *Process Saf. Environ. Prot.* **2020**, *139*, 297.

[67] T. Shang, Z. Lin, C. Qi, X. Liu, P. Li, Y. Tao, Z. Wu, D. Li, P. Simon, Q. H. Yang, *Adv. Funct. Mater.* **2019**, *29*, 1903960.

[68] H. Zhuo, Y. Hu, Z. Chen, X. Peng, L. Liu, Q. Luo, J. Yi, C. Liu, L. Zhong, *J. Mater. Chem. A* **2019**, *7*, 8092.

2008006 (12 of 12)